PHYSICAL REVIEW E **73**, 041508 (2006)

Minimal model for chaotic shear banding in shear thickening fluids

A. Aradian* and M. E. Cates
SUPA, School of Physics, University of Edinburgh, JCMB Kings Buildings, Edinburgh EH9 3JZ, United Kingdom

(Received 12 October 2005; revised manuscript received 13 February 2006; published 18 April 2006)

We present a minimal model for spatiotemporal oscillation and rheochaos in shear thickening complex fluids at zero Reynolds number. In the model, a tendency towards inhomogeneous flows in the form of shear bands combines with a slow structural dynamics, modeled by delayed stress relaxation. Using Fourier-space numerics, we study the nonequilibrium "phase diagram" of the fluid as a function of a steady mean (spatially averaged) stress, and of the relaxation time for structural relaxation. We find several distinct regions of periodic behavior (oscillating bands, traveling bands, and more complex oscillations) and also regions of spatiotemporal rheochaos. A low-dimensional truncation of the model retains the important physical features of the full model (including rheochaos) despite the suppression of sharply defined interfaces between shear bands. Our model maps onto the FitzHugh-Nagumo model for neural network dynamics, with an unusual form of long-range coupling.

DOI: 10.1103/PhysRevE.73.041508 PACS number(s): 83.10.−y, 82.70.−y, 05.45.−a, 83.60.Wc

I. INTRODUCTION

Complex fluids have long been known to show strong coupling between structure and flow. This leads to viscoelasticity in both the linear and the nonlinear response. The latter can include both shear thinning and shear thickening, with upward and downward curvature, respectively, in the steady state flow curve $\sigma(\dot{\gamma})$ of shear stress against strain rate. Polymers are usually shear thinning, whereas viscoelastic micellar systems can be either thinning or thickening, as can dense colloidal suspensions [1,2]. In extreme cases of shear thinning, where $\sigma(\dot{\gamma})$ becomes nonmonotonic, steady flow is mechanically unstable on the decreasing portion of the curve. Stability can sometimes be restored by shear-banding, in which bands of material with unequal strain rate $\dot{\gamma}$ but equal stress σ coexist, with interface normals in the shear gradient direction [3,4]. For extreme shear thickening, the same applies interchanging σ and $\dot{\gamma}$, with band interface normals now in the vorticity direction [5,6].

It has recently become clear, however, that in some complex fluids (as outlined below) parameter regimes exist where the constitutive response to steady driving is intrinsically unsteady. This entails a different (or at least stronger) dynamical instability to the one present in shear-banding. These instabilities are not transient phenomena: They rather indicate the presence of complicated dynamical states within the flow diagrams of complex fluids. In principle there can be many sources of dynamical instability: Under appropriate conditions, complex fluids—like simple fluids—are subject to classical inertial (Taylor-Couette, turbulence) or thermoconvective (Rayleigh-Bénard) instabilities [7,8]. More specific to complex fluids are stick-slip phenomena (like the "spurt" or 'melt fracture' effect [1]) and various elastic instabilities (so-called "elastic turbulence" [9]).

Here we address a distinct class of instabilities in which not only the mechanical response, but also the internal structural parameters of the fluid, vary in time. Experimentally, such structural instabilities arise in a variety of systems. Typical observations fall into two broad types.

The first type of unstable temporal behavior comprises sustained, periodic oscillations of the shear rate at constant imposed shear stress, or vice versa: This has been observed for surfactant solutions either in worm-like micellar phases [10–14] or lamellar phases [15–18], as well as in polymer solutions [19] and concentrated colloids [20]. The second type of unsteady behavior is more complex, with erratic temporal responses of either the shear rate or shear stress. Such irregular signals have been observed in worm-like micelles [21–24], lamellar (onion) phases [16,17,25] and concentrated colloids [26]. In many of these systems, such erratic responses occur for parameter values enclosed within those where oscillations arise.

There are strong indications [16,21,22] that these erratic responses result from a deterministic chaotic dynamics. A remarkable aspect of chaos in these flows is that the Reynolds number is virtually zero: The inertial term $\boldsymbol{v}.\nabla\boldsymbol{v}$ in the Navier-Stokes equation is negligible. The instabilities thus stem from constitutive nonlinearity in the rheology of the fluid, unlike the convective instability that gives rise to turbulence in Newtonian flows. The term "rheological chaos," or simply "rheochaos" has been coined for such behavior [27].

The involvement of the fluid microstructure in these instabilities was established by monitoring structural observables and showing that these evolve in concert with the time-dependent rheological signal. The methods used include birefringence imaging [11,19], light scattering [15,16] and spatially resolved nuclear magnetic resonance (NMR) [24]. Many (but not quite all) instances of structural instability occur in shear-stress or shear-rate ranges close to nonequilibrium transitions between distinct phases or textures in the fluid, for example, the transition from isotropic to flow-aligned-nematic structures in worm-like micelles [24], or the disordered-to-layered packing transition in multilamellar on-

---

*Also at Centre de Recherche Paul Pascal, CNRS, Avenue A. Schweitzer, 33600 Pessac, France. Electronic address: aradian@crpp-bordeaux.cnrs.fr ions [15–17,25]. (There may also be underlying transitions from a flowing to a jammed state in colloids [26], and from isotropic to string-like structures in polymer solutions [19].) Structural instabilities arguably arise when the fluid under flow hesitates between possible alternative structures near such transitions.

A crucial question is whether structural instabilities are purely temporal or spatiotemporal in character. Do all points in the fluid follow the same time evolution, or do different parts of the fluid have different mechanical and structural states at the same instant of time? Early experiments on worm-like micelles [11,12] and polymers [19] pointed towards heterogeneity: Optical observations showed alternating turbid and clear bands. More recent advances allow spatially and temporally resolved measurements of velocity profiles within a rheometer. Such experiments, on multilamellar onions [17,25] and worm-like micelles [24], unambiguously demonstrate both the presence and the nature of the heterogeneities: They are *fluctuating shear bands*. Theoretical models that address only temporal instability in a spatially uniform system, such as that of Ref. [27] are, therefore, of limited relevance to the experimental situation.

In this paper we extend the model of Ref. [27] to allow for spatial heterogeneity, exploring the resulting scenario of why shear bands destabilise in such fluids and how this produces oscillatory and chaotic flows. (Note that we work in a parameter regime where the flow curve is monotonic, so that shear bands cannot exist as a time-independent steady state.)

We thereby create a minimal model of spatiotemporal instabilities in shear-thickening fluids. The model includes an intrinsic short-time tendency to form shear-bands coupled to a slow relaxational component dynamics for the fluid microstructure (modeled as a retarded stress response term). In the purely temporal model of Ref. [27], oscillations but not chaos were found (unless a physically unconvincing "double memory" term was used). By allowing for full spatiotemporal dynamics, we show that the interplay between the above two factors gives rise to several distinct periodic regimes (including oscillating shear bands and traveling bands) and also regimes of spatiotemporal rheochaos. Preliminary accounts of our work were given in Refs. [28,29].

Our motivation for studying the case of a fluid that shows shear-thickening (in itself a widely observed but poorly understood phenomenon [30,31]) is that several of the above-cited experiments concern such fluids (Refs. [10–13,22] for wormlike micelles; [19] for polymer solutions; and [20,26] for colloidal suspensions).

The alternative case of shear-thinning fluids has been recently addressed by Fielding and Olmsted [32], and in less detail also by ourselves [29]. The authors of Ref. [32] have demonstrated the presence of a rich dynamics, including rheochaos, in their model. Also closely related is the work by Chakrabarti *et al.* [33] on nematic liquid crystals which also shows regimes of spatiotemporal chaos. In what follows, we shall note similarities and differences between our own work and these other studies.

The rest of this paper is organized as follows. In Sec. II, we define the model, discuss its physical assumptions, and relate it to other models (both in rheochaos and in other fields of study). In Sec. III, we give a qualitative description of how the model works. Section IV explains how the model is solved numerically. In Sec. V, we present our results in the form of a nonequilibrium "phase diagram" and comment on the various flow regimes encountered. Section VI studies a low-dimensional version of the model which offers further insights into the nature of rheochaos. In Sec. VII we summarize our findings and their generic implications for the physics of rheological instabilities in complex fluids.

II. THE MODEL

Our model has two main physical ingredients, as follows:

(i) The fluid has a tendency to form shear bands;

(ii) there are slow structural modes in the fluid whose delayed relaxation modifies the evolution of the stress.

The latter ingredient is central to our description. When some structural mode is disturbed by the flow, it will relax on a timescale that is distinct from the stress relaxation time in the system. Below, for simplicity, we will consider a single timescale τ_S for structural relaxation, with stress relaxation assimilated into the usual Maxwell time τ_M. We focus on the case where structural modes relax at least as slowly as the stress itself would do at fixed structure ($\tau_S > \tau_M$).

Because of the disordered energy landscape and metastability intrinsic to many complex fluids [34–36], such slow dynamics is commonplace. Candidates for slow structural modes include the mean length or the local gel fraction in worm-like micelles; local composition variables (e.g., colloidal volume fraction); and "fluidity" parameters reflecting, e.g., a local bonding state [29,37]. An involvement of slowly evolving structure has been shown in many experimental cases [10–19].

A. Model equations

We consider the situation of a fluid under pure shear, and we assume, as usual [2], that the shear stress σ decouples from other stress components, and depends only on the rate of shear strain $\dot{\gamma}$. We will restrict our study to one-dimensional spatial heterogeneity in the fluid, in the vorticity direction (perpendicular both to the velocity and the velocity gradient); in cylindrical Couette geometry, which we will always refer to in the following, this corresponds to the axial coordinate denoted z. [For three-dimensional (3D)-related effects in situations of shear-banding, see [38].]

This choice for the heterogeneity direction is motivated by the classical geometry of steady shear bands in thickening materials [5,6] where, as shown in Fig. 1, bands are stacked one onto another in the vorticity direction (vorticity shear bands). Note that, under these assumptions, the shear flow is homogeneous within each slice of height z, as required by the low-Reynolds limit. (We neglect any small variation in the velocity gradient direction caused by the curvature of the cell. Without fluid inertia, the stress cannot vary in this direction.)

In all of the following, we shall work under conditions of imposed torque, i.e., under an imposed value of the mean (spatial average) of the stress $\langle\sigma\rangle$: This is the usual situation for vorticity shear bands, shown in Fig. 1. [We also studied

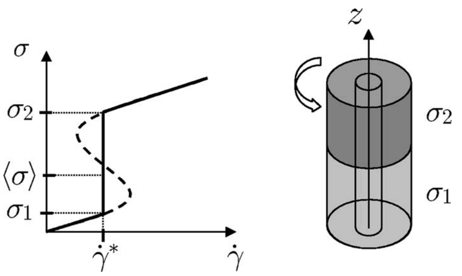

FIG. 1. Vorticity shear bands in a Couette cell [5,6]. These occur in shear thickening materials with an S-shaped flow curve (σ vs $\dot\gamma$). A given mechanical torque on the Couette imposes a mean (spatially averaged) stress $\langle\sigma\rangle$. Any $\langle\sigma\rangle$ within the unstable portion of the flow curve is unstable toward shear bands (with different local microstructures) along the vorticity direction z, depicted here as a clear and a turbid band. These coexist at a common shear rate $\dot\gamma_c$ (whose value is fixed by gradient terms [4]) but at different stresses σ_1 and σ_2. The amount of each band is such that the weighted mean of σ_1 and σ_2 matches the externally imposed mean $\langle\sigma\rangle$.

the behavior of our model under conditions of imposed shear rate (results not shown) but no spatiotemporal effect was observed, see note [39].]

In our model, the shear stress $\sigma(z,t)$ at time t evolves according to the following equation of motion:

$$\dot\sigma(z,t) = \dot\gamma(t) - R(\sigma) - \lambda \int_{-\infty}^{t} \mathcal{M}(t-t')\sigma(z,t')dt' + \kappa\nabla^2\sigma \tag{1}$$

where

$$R(\sigma) = a\sigma - b\sigma^2 + c\sigma^3 \text{ and } \mathcal{M}(u) = \frac{1}{\tau_S} e^{-u/\tau_S} \tag{2}$$

Equations (1) and (2) are nondimensional: The transient elastic modulus is taken as the unit for stress, and H, the axial extent of the Couette cell (vertical in Fig. 1), the unit of length. Several choices are possible for the time unit; the simplest one is the fluid's Maxwell time τ_M. However, as we will always be dealing with times longer than τ_M, we choose instead $100\tau_M$ as a time unit. [This amounts to setting $\tau_M = 0.01$ and, via Eq. (3), $a=100$ throughout what follows; we do this.] The reader is referred to Appendix A for details on the nondimensionalization procedure.

Note that $\dot\sigma = \partial\sigma/\partial t$ in Eq. (1) is a local time derivative. We also emphasize that the shear rate $\dot\gamma$ in Eq. (1) is *uniform*: The moving wall of the rotor imposes the same velocity for all heights z, and $\dot\gamma(z,t) = \dot\gamma(t)$ only.

The terms in Eqs. (1) and (2) have the following significance. $R(\sigma)$ describes instantaneous, nonlinear stress relaxation. As defined by Eq. (2), R is a third-order polynomial, with the positive constants a, b, and c chosen so that $R(\sigma) > 0$ for $\sigma > 0$, and so that the inverse function, $\sigma(R)$, is an S-shape (see Fig. 2). We choose $a=100$, $b=20$, $c=1.02$ in this paper; setting $c=1$ would give a physically inappropriate zero of $R(\sigma)$ at $\sigma=10$. The $R(\sigma)$ term encodes ingredient (i) of the model, i.e., the tendency of the fluid to form vorticity shear-bands. This tendency is instantaneous, but frustrated by structural relaxation effects—see Fig. 3. Note that, with our choice of units, a controls linear stress relaxation in the fluid, and hence determines the Maxwell time τ_M:

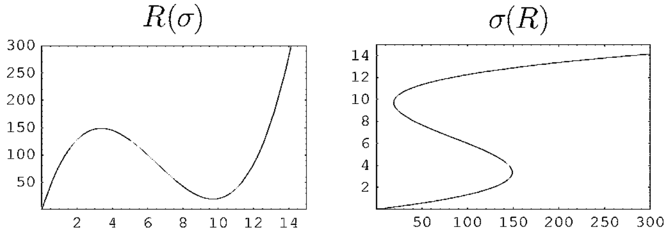

FIG. 2. Plots of $R(\sigma)$ and the inverse function $\sigma(R)$. The S-shape of the latter encodes the tendency of the fluid to form vorticity shear bands.

$$\tau_M = 1/a \tag{3}$$

Setting $b=c=\lambda=\kappa=0$ in Eq. (1) indeed recovers the classical Maxwell model for linear viscoelasticity.

The integral term in Eq. (1) corresponds to our second physical ingredient, and represents retarded stress relaxation due to slow structural reorganisation in the fluid; λ is a positive constant governing the strength of this term. For the sake of simplicity, retarded relaxation is chosen linear in past stresses; but note that, as discussed in Ref. [27], a similar form can be obtained by introducing an explicitly structure-dependent $R(\sigma)$ and then linearizing this structure-dependence. The memory kernel $\mathcal{M}$ is in principle any decaying function [27]. However, in Eq. (2), we choose it mono-exponential with characteristic time τ_S. This choice permits a much simpler, fully differential representation that we exploit in our numerics below. As stated previously, we take structural relaxations to be slow compared to the intrinsic time scale of stress relaxation; we study mainly $4 < \tau_S/\tau_M < 10^4$. (This contrasts somewhat with the model of Ref. [32] where $\tau_S/\tau_M \simeq 1$.)

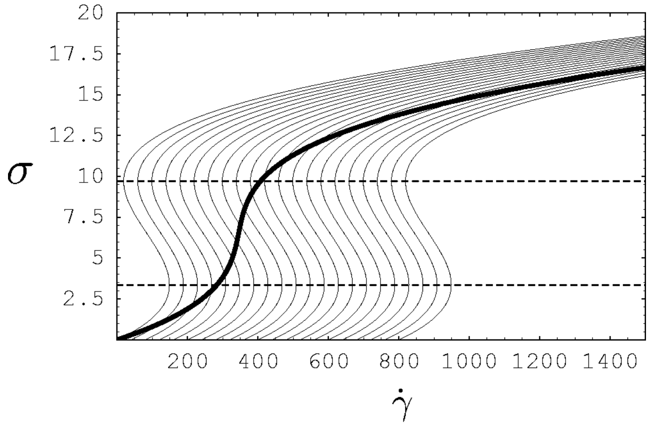

FIG. 3. Steady-state flow curve (thick line), and underlying short-term flow curves (thin lines, with, from left to right, $m = 0,1,2,\ldots,20$). The stress range between the dotted lines corresponds to the unstable region, here deduced for $\tau_S=100$ from Eq. (9). Numerical parameters: $\lambda=40$, $a=1/\tau_M=100$, $b=20$, $c=1.02$, $\kappa=0.01$, $H=1$.

Finally, the last term of Eq. (1) assigns to stress a diffusivity κ. By analogy with the classical Cahn-Hilliard model for phase separation [40], this can be viewed as representing the cost of maintaining interfaces in inhomogeneous states. Such minimal nonlocality in the constitutive model is known to be physically crucial. For example, in steady-state shear bands it drives a selection mechanism, among all possibilities on a given flow curve like that of Fig. 1, for the coexistence strain rate $\dot{\gamma}_{\mathrm{c}}$ [4].

A superficial comparison of Eq. (1) with Ref. [27] might suggest that our work is new only in the addition of this diffusive term. But of course we simultaneously upgrade the dimensionality of the problem from $\sigma(t)$ in that work to $\sigma(z,t)$ here; this allows vastly richer behavior, in better correspondence with the experimental facts, to emerge.

We now recast Eqs. (1) and (2) into a purely differential form [27]. We define a new variable

$$m(z,t) = \int_{-\infty}^{t} \mathcal{M}(t-t')\sigma(z,t')dt' \tag{4}$$

which we call the "memory," and which contains the structural part of the stress relaxation. We can then rewrite Eq. (1) as an exactly equivalent differential system

$$\dot{\sigma} = \dot{\gamma} - R(\sigma) - \lambda m + \kappa \nabla^2 \sigma \tag{5}$$

$$\dot{m} = -\frac{m-\sigma}{\tau_{\mathrm{S}}}. \tag{6}$$

Equation (6) states that the memory is always relaxing towards the current and local value of the stress $\sigma(z,t)$ with a (slow) rate τ_{S}^{-1}.

In its differential form, the model can be interpreted as follows. Equation (5) is a nonlinear rheological equation controlling the temporal evolution of the stress, where one of the participating variables is structural by nature (the memory m); this structural variable is subject to a distinct dynamics, governed by a "structural equation," Eq. (6), with a different relaxation time τ_{S}. The coupling of the two dynamics, mechanical and structural, is the source of the instability.

B. Relation to other models

Viewed in this way, our model belongs to a larger class of models that have been recently proposed to describe the dynamics of complex fluids.

The models of Refs. [32,29] for shear-thinning solutions of worm-like micelles work on a similar scheme: there, the "structural variable" is the mean chain length of the micelles [32], or simply the Maxwell time of the fluid itself [29]. In both cases, its evolution is governed by a differential "structural equation" akin to Eq. (6). Belonging to the same family, albeit coming from a somewhat different perspective, Derec *et al.* proposed a model for the fluidization transition in pastes [37], where a classical rheological equation is supplemented by a structural equation describing a "fluidity" parameter.

From a more formal point of view, all these models are related to the prey-predator and reaction-diffusion models commonly found in nonlinear physics and mathematical biology [41]. (In our case, σ and m are the two competing species.) This type of nonlinear models are known to yield complex spatiotemporal behavior [41], thus it should not come as a surprise that the related models used in the field of complex fluids do also.

It is interesting to note that our Eqs. (5) and (6) in fact map exactly onto a well-known model of nonlinear physics, the FitzHugh-Nagumo model [41–45]. The simplest version of the latter model was developed to describe electrical activity in a single neuron, where the axon membrane potential is a fast variable (also called "excitation variable," analogous to σ in our model), and is coupled to the dynamics of a slow variable (or "recovery variable," analogous to m), related to the activity of sodium ion channels. This system is known to produce van-der-Pol-like (purely temporal) oscillations, like those described for complex fluids in the earlier, spatially homogenized, version of our model [27].

In recent years, spatially inhomogeneous extensions of the FitzHugh-Nagumo have been used to study the collective properties of interacting networks of neurons, and other related assemblies of coupled nonlinear oscillators, focussing on the competing effect of local and global couplings [46–49]. The model of Eqs. (5) and (6) is of just this type: The local coupling is supplied by the diffusion term $\kappa\nabla^2\sigma$, and the global coupling by the constraint that the spatial mean stress $\langle\sigma\rangle$ is externally fixed.

We remark, however, that: (a) In our model, the mean value of the stress is fixed, while in neural networks where a coupling to the mean membrane potential is implemented [46,48,49], its value fluctuates in response to the collective dynamics in the model; (b) possibly for this reason, several of the spatiotemporal patterns reported below (in particular oscillatory shear bands) have not to our knowledge been reported in the literature on FitzHugh-Nagumo networks; (c) an active research topic in neural networks is the effect of noise on global behavior, including the possibility to trigger chaotic dynamics [49]. Such a role for noise (either thermal, or mechanical) is neglected in most models of rheochaos but would constitute an interesting avenue for future research.

III. QUALITATIVE FEATURES

We now explain some qualitative features of our model, focusing on the origin of the dynamical instability, and on a physically important scaling property. We also briefly discuss how the values of our model parameters may be estimated from experiment.

A. Flow curves

We start by computing the flow curves for the fluid, i.e., the relation between σ and $\dot{\gamma}$ in steady-state flow.

From Eqs. (5) and (6), the flow curve for steady-state, homogeneous flows is given by setting $\dot{\sigma}=\dot{m}=\nabla^2\sigma=0$. Equation (6) then yields $m=\sigma$: At each point on the curve, the memory has relaxed to the steady-state stress. This can be substituted in Eq. (5), to provide the equation for the steady-state flow curve [27]:

$$\dot{\gamma} = R(\sigma) + \lambda\sigma. \tag{7}$$

When $R'(\sigma)+\lambda \geqslant 0$ for all values of σ (a condition which we shall always take to hold below) the flow curve is monotonically increasing, as in the thick curve in Fig. 3. In contrast with rheological constitutive models that do not show structural coupling, this monotonicity does not ensure mechanical stability of homogeneous flows [27].

The qualitative reason for instability of the monotonic flow curve is that the steady states associated to this curve only arise when the memory m has relaxed, i.e., for time scales beyond τ_S. For times much shorter than τ_S, the fluid instead behaves as if the memory m was frozen. Thus, at short time scales, the fluid lives on one of a set of "instantaneous flow curves" for which stress has relaxed, but not structure. These instantaneous curves have $\dot{\sigma}=0$ at fixed m, giving

$$\dot{\gamma} = R(\sigma) + \lambda m \text{ (short term)}, \tag{8}$$

where m is a parameter. Such curves for $m=0,\ldots,20$ are plotted in Fig. 3, and are not monotonic. As the memory slowly relaxes, the fluid drifts from one such curve to another; Eq. (7) can be reconstructed by picking, for each value of the stress σ, the corresponding point on the particular instantaneous curve that has $m=\sigma$. But for our choice of nonmonotonic R, the fluid has an instantaneous tendency to form shear-banded flow. This impedes the establishment of a steady state and instability can arise even when the steady-state flow curve is monotonic [27].

B. Origins of the dynamical instability

As just discussed, the existence of decreasing portions of the short-term flow curve, in contradiction with the steady-state flow curve, is a source of instability. In the homogeneous version of the model (no z-dependence), this causes temporal instability in the form of van-der-Pol-type oscillations [27]. Essentially, the mechanism for such oscillations is as follows: Starting, For instance, from a situation of high stress as compared to the memory ($\sigma > m$), the memory m will start to grow as dictated by Eq. (6); this growth of m in turn brings a decrease in the value of σ through Eq. (5); adapting to this, m then decreases, which increases σ, thereby recovering the initial high-stress situation and starting the cycle anew.

When spatial dependence is added, this basic temporal oscillation becomes compounded with shear banding. It is easily seen how this can give complex spatiotemporal dynamics: looking at Fig. 3, if one imposes a mean stress $\langle\sigma\rangle$ chosen within the unstable region, the system decomposes into several shear bands with unequal local stress, as depicted on Fig. 1. Unlike the classical situation of Fig. 1, here the van-der-Pol-type temporal oscillation rules out steady states for the shear bands: a local unstable dynamics engages. Simultaneously, the bands have to match, all together, the constraint on $\langle\sigma\rangle$. This creates long-range couplings between the bands (when one oscillates, another has to compensate), considerably complicating the spatiotemporal behavior.

C. Linear stability analysis

We have performed a standard linear instability calculation on models (5) and (6), with the following results:

(i) For an externally imposed value of the mean stress $\langle\sigma\rangle$, instability for stress evolution arises only if

$$R'(\langle\sigma\rangle) + \frac{1}{\tau_S} < 0. \tag{9}$$

(ii) when the above instability condition is obeyed, only stress modes with wavevectors q in the range

$$0 \leqslant q \leqslant \sqrt{-\frac{R'(\langle\sigma\rangle)+1/\tau_S}{\kappa}} \tag{10}$$

are unstable. Also, modes with smaller wavevectors have a larger growth rate: When the uniform $q=0$ mode is constrained, the lowest nonzero q-mode grows fastest.

The instability condition (i) is the same as for the purely temporal version of the model [27]; it states that instability can arise only in regions of decreasing R (or equivalently, within the decreasing portions of the short-term flow curves in Fig. 3), and that it is facilitated as τ_S becomes larger or impeded as it becomes shorter.

The second result (ii) is a natural consequence of stress diffusion with diffusivity κ; this kills off fluctuations with too large q (small wavelengths) and prevents such modes from becoming unstable.

D. Scaling property of the model

Let us assume that a stress response $\sigma(z,t)$ and shear rate $\dot{\gamma}(t)$ are obtained as the solutions of the model of Eqs. (5) and (6), under conditions of imposed mean stress $\langle\sigma\rangle$ and with a given set of parameters $a=\tau_M^{-1}, b, c, \lambda, \tau_S, \kappa$. Then, choosing any scaling factor α, the scaled responses $\alpha\sigma(z,t)$ and $\alpha\dot{\gamma}(t)$ would also be obtained as the solutions of the model if one applied a mean stress $\alpha\langle\sigma\rangle$ and used a scaled set of parameters $a=\tau_M^{-1}, b/\alpha, c/\alpha^2, \lambda, \tau_S, \kappa$.

The proof of this scaling property is elementary and left to the reader. It means that, although all numerical results given below are found with one specific set of model parameters ($\lambda=40$, $a=1/\tau_M=100$, $b=20$, $c=1.02$, $\kappa=0.01$, $H=1$), they in fact describe the behavior of a one-parameter manifold of parameters governed by the scale transformation parameter α.

Secondly, for our chosen parameter set, the observed stresses in both oscillatory and chaotic regimes are very large (of order 10 in dimensionless units, i.e., ten times the elastic modulus of the fluid). While such large amplitudes of the elastic strain may be relevant for certain types of fluids, no direct importance should be attached to this: One can scale down numerical values of the stress to around, say, unity, keeping exactly the same oscillatory or chaotic dynamics. Note, however, that this will not change the ratio of stress fluctuation to mean stress; this is always large for our parameter settings. (The parameter space is vast, and we have not explored values for which this ratio might be reduced.)

E. Experimental estimates for model parameters

Our model involves a set of phenomenological model parameters whose numerical values are *a priori* unknown. One way around this difficulty is try to extract estimates for these values using appropriate experiments: It is thus useful, at this point, to sketch some of the possible strategies—keeping in mind, however, that our minimal model is intended essentially for a qualitative exploration of the physics at work in complex fluids not for an effective fitting tool for specific nonlinear materials.

(It is also recalled that numerical values used in the article are nondimensional; see Appendix A for the procedure to convert dimensional quantities, as obtained from experiments, to nondimensional ones.)

A first experimental strategy is as follows: Starting from a state of complete rest (where the structural memory has fully relaxed, $m=0$), and assuming that the structural time τ_S is slow enough, one may be able to measure the instantaneous flow curve at zero memory [Eq. (8)] using a moderately rapid ramp up of the applied stress (e.g., sample the whole curve within a few minutes). Of course, the obtained curve would be unstable (Fig. 3), showing a conventional "discontinuous shear-thickening" scenario with a shear-rate plateau and classical (steady-state) shear bands; but the information collected on the plateau (critical shear rate, lower and upper values of the stress at the jump, …) would probably be sufficient to estimate the short-term parameters a, b, c, and thereby determine the function $R(\sigma)$ in the model.

Following this determination of R, the value of the coupling parameter λ could then be found through a simple steady-state experiment where a constant stress σ_{ss} is imposed for a long period a time (in a stable region of the phase diagram): As stated by Eq. (7), the shear rate then corresponds to the (known) instantaneous contribution $R(\sigma_{ss})$ plus the delayed contribution $\lambda\sigma_{ss}$. Thus, a measure of the shear rate will determine the value of λ, the only unknown in the equation.

Next, estimating the value of the structural relaxation time τ_S could be done through a relaxation experiment: From a situation of steady state under a given applied stress, the value of the stress is suddenly changed to a new constant value (or even cancelled); if τ_S is long compared to other times in the system, it should be controlling the global relaxation of the response to the new steady state. Another possibility which could be explored could be to look at the linear viscosity after a period of strong shear and/or after a temperature jump [31].

The last parameter that needs to be determined is the stress diffusivity κ, which in classical, steady-state shear banding is related to the width of the interfaces between bands. We expect κ to be extremely small [50] (and in any case, much below the artificially large value of 10^{-2} used throughout this work for computing reasons), although we are not aware of any experiments allowing to measure it. This should not be too much of an issue, as our results show that (below a certain threshold) the behaviour of the model does not qualitatively depend on the actual value of κ.

IV. NUMERICAL METHODS

In this section, we detail the numerics techniques used to obtain the results presented in the rest of the article.

A. Spectral scheme; boundary conditions

Our numerical scheme expands the stress in Fourier modes, then is solving for the evolution of these—rather than directly solving the model equation on a grid of points in direct space [32,33]. Such a spectral scheme [51] had two main advantages, as follows: (a) In Fourier space, working under conditions of fixed mean stress simply corresponds to fixing the value of the uniform, zeroth mode in the Fourier expansion of the stress (this is much more difficult to implement in direct-space schemes); (b) Not only can arbitrarily accurate numerical results be obtained by keeping enough Fourier modes in the scheme ("high-order truncation"), but also, by keeping only a minimal number of modes ("low-order truncation"), one can obtain a reduced description whose analysis is much simplified. Such a truncation is more likely to capture the physics of the problem than a reduced real-space scheme with a spatial grid of only a few points. We shall present both high-order and low-order numerics in what follows.

We must also choose appropriate boundary conditions on the system. We demand zero stress flux at both ends of the Couette cell:

$$\nabla \sigma\big|_{z=0} = \nabla \sigma\big|_{z=H} = \mathbf{0}. \tag{11}$$

To motivate this, note that stress flux arises through the diffusion term in Eq. (5), which is generally ascribed to material displacement of stress-carrying elements [52]. Our boundary conditions then reflect the fact that no fluid element leaves through the top nor bottom of the cell.

Now recall that, for reasons related to the physics of vorticity shear banding (Fig. 1), we have the constraint:

$$\langle\sigma\rangle = \frac{1}{H}\int_0^H \sigma(z,t)dz = \text{const}. \tag{12}$$

We now decompose the stress field onto a Fourier basis of spatial modes compatible with the above boundary conditions (cosines only):

$$\sigma(z,t) = \sum_{k=0}^{N-1} \sigma_k(t)\cos(k\pi z/H) \tag{13}$$

and note that $\sigma_0(t)=\langle\sigma\rangle$ (given that $H=1$ in our units). Similarly for the memory term:

$$m(z,t) = \sum_{k=0}^{N-1} m_k(t)\cos(k\pi z/H). \tag{14}$$

The series in Eqs. (13) and (14) only contain the first N modes $\sigma_k(t)$ and $m_k(t)$ of an infinite Fourier series: The level N of this truncation (known as a Galerkin truncation [51]) determine the overall accuracy of the scheme. (For a given accuracy, the number of modes that must be kept is often much lower than the number of grid points in any real-space discretization [51].)

We now project Eqs. (13) and (14) onto the Fourier basis to obtain a set of evolution equation for each of the mode amplitudes $\sigma_k(t)$ and $m_k(t)$. Thanks to the simple functional form of the model, it is possible to obtain analytical expressions for the mode equations, which are given in full in Appendix B. These mode equations are of the form ($1 \leqslant k \leqslant N-1$)

$$\dot{\sigma}_k = (\text{coupling terms}) - \lambda m_k - \kappa q_k^2 \sigma_k \tag{15}$$

$$\dot{m}_k = -\frac{m_k - \sigma_k}{\tau_\mathrm{S}} \tag{16}$$

where $q_k = k\pi/H$ is the wavevector, and the coupling terms, stemming from the nonlinearity of the instantaneous term $R(\sigma)$, link the evolution of each σ_k mode to all others. As expected, stress diffusivity damps higher modes via a linear κq^2 term.

Finally, the equations for the $k=0$ uniform modes $\sigma_0(t) = \langle\sigma\rangle$ and $m_0(t)$ are

$$\dot{\sigma}_0 = 0 = \dot{\gamma}(t) - \frac{1}{H}\int_0^H R[\sigma(z,t)]dz - \lambda m_0(t) \tag{17}$$

$$\dot{m}_0 = -\frac{\langle\sigma\rangle - m_0(t)}{\tau_\mathrm{S}}. \tag{18}$$

Integrating Eq. (18) gives [with $m(t=0)=0$, see below]

$$m_0(t) = \langle\sigma\rangle(1 - e^{-t/\tau_\mathrm{S}}). \tag{19}$$

Plugging this expression into Eq. (17), we obtain an important expression which provides us with the instantaneous value of the shear rate $\dot{\gamma}$, once the value for the stress has been calculated from the Fourier modes:

$$\dot{\gamma}(t) = \frac{1}{H}\int_0^H R[\sigma(z,t)]\mathrm{d}z + \lambda\langle\sigma\rangle(1 - e^{-t/\tau_\mathrm{S}}). \tag{20}$$

The spatial integral in this expression can in fact be carried out analytically, not numerically (see Appendix B).

The final outcome of the Fourier-Galerkin truncation scheme is that the partial differential equations (5) and (6) in the original formulation of the model have become a dynamical system of finite order, containing $2N$ ordinary differential equations for the modes $\sigma_k(t)$ and $m_k(t)$ as specified by Eqs. (15) and (16), plus the above equations for the uniform modes. The numerical integration of the ordinary differential equations (15) and (16) was performed with the help of a commercial solver package [53], using an adaptive time step. Given the separation of scales between the typical times τ_M and τ_S, the adaptive step was needed, to maintain acceptable computing times.

Initial conditions at $t=0$ were chosen as follows: Memory was set to zero [i.e., $m_k(0)=0$ for all k], and initial values for each stress mode $\sigma_k(0)$ were picked at random between 0 and 10^{-4}. The noise amplitude was found not to be essential to the qualitative results obtained.

B. High-order and low-order truncation

The behavior of our fluid model was explored using two types of Fourier-Galerkin schemes: One where the number of modes kept in Eqs. (13) and (14) is high ($N=40$), and one where it is minimal ($N=3$).

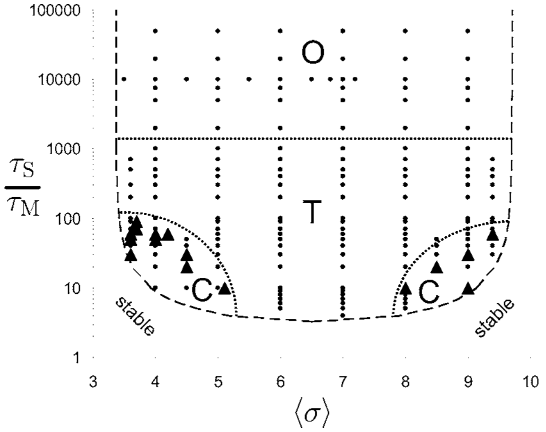

FIG. 4. Phase diagram of the model when τ_S and $\langle\sigma\rangle$ are varied: (▲) chaotic (●) periodic point. Three main regimes are observed: (O) oscillating shear bands, (T) traveling shear bands, (C) chaotic regions. The outer dashed line is the linear stability limit, $R'(\langle\sigma\rangle) + 1/\tau_\mathrm{S} = 0$ [Eq. (9)]. Numerical parameters as in Fig. 3.

For the high-order truncation (Sec. V), we found that keeping $N=40$ modes was numerically accurate, with reasonable computing times. One criterion in this choice was that numerics should be able to fully resolve interfaces between shear bands (the sharpness of interfaces is essentially controlled by the stress diffusivity κ; we set it to 10^{-2} unless otherwise stated). A second criterion is that N should be high enough that results become N-independent: This was indeed the case, with truncations from $N=25$ up all giving similar outputs. This applies at the level of phase diagrams, etc., but not to individual trajectories which (at least in chaotic regions of the phase diagram) can depend on every detail of the numerics.

We also checked the validity of our high-resolution results, for a given set of parameters, against variations in either initial conditions for the stress modes, or in the actual sequence of time steps followed by the adaptative iterator during numerical integration. We found a limited dependence on these factors from one run to another. To take this into account, the "phase diagram" of Fig. 4, where the general behavior of the model is summarized, was established on the basis of several independent runs for each point marked in the figure. Thus the general features of the phase diagram, as well as all conclusions drawn on the model's global behavior, are reliable.

In the low-order truncation (Sec. VI), on the other hand, our aim was to study the behavior of the model in its simplest possible spectral representation. In particular, we are interested in whether low-dimensional chaos was present and what route led to it. Since three degrees of freedom are required to allow for chaos, the lowest compatible truncation in our model corresponds to $N=3$: Excluding uniform modes $\sigma_0 = \langle\sigma\rangle$ and m_0, which are dynamically inactive, this leaves a four-dimensional system involving σ_1, σ_2, m_1, and m_2. In the following sections, we present the results of the model, first in the high-order truncation, then in the low-order.

V. HIGH-ORDER RESULTS

In this section, we present the results that were obtained by solving the model of Eqs. (15) and (16) in the high-resolution truncation ($N=40$).

A. Phase diagram

To get a global picture of the model's behavior, we made a systematic exploration of its spatio-temporal dynamics by varying the two physically most important parameters: The ratio between the structural timescale and the mechanical timescale τ_S/τ_M, and the spatially averaged stress $\langle\sigma\rangle$ (fixed by the mechanical torque on the Couette). On varying τ_S/τ_M, we choose to keep τ_M fixed ($\tau_M=1/a=0.01$) and vary τ_S only. All other parameters are held at their values of Fig. 3, i.e., $b=20$, $c=1.02$, $\lambda=40$, $\kappa=0.01$, $H=1$.

Despite the high-dimensional dynamical system under consideration ($2N=80$), the obtained "phase diagram" for the model (shown in Fig. 4) displays a simple overall structure where three main dynamical regimes emerge: Periodic response with (more or less complex) oscillating shear bands at extremely long τ_S; periodic response with traveling bands for long τ_S; and finally, chaotic response at shorter τ_S and off-centered values of $\langle\sigma\rangle$. The dotted lines separating regions on the phase diagram are guides to the eye, representing cross-overs not sharp transitions between different types of behavior. The "C-regions" marked in the plot were defined so as to enclose all observed chaotic points; these regions do, however, contain internal structure with periodic and chaotic pockets, whose exact boundaries can depend on initial conditions and other details.

We next discuss in some detail the three main regimes encountered on the phase diagram, emphasizing an intuitive understanding of the physics involved. However, as shall be seen, there is significant variety in behavior even within the same regime.

1. Periodically oscillating shear bands

We first discuss the regime encountered when structural evolvution is much slower than stress relaxation (typically $\tau_S/\tau_M \geqslant 10^3$) marked "O" in Fig. 4. Here periodic oscillations of the shear rate and stress are observed, while spatially, the flow presents oscillating shear bands. Depending on the imposed stress $\langle\sigma\rangle$, the waveforms of these band oscillations [which induce oscillations in both the local stress $\sigma(z,t)$ and the mean strain rate $\dot{\gamma}(t)$] range from simple to very complex. Moving along any horizontal line within the region O (changing $\langle\sigma\rangle$ at constant τ_S/τ_M), one observes the same succession of behaviors; we present these for one typical line, $\tau_S/\tau_M=10^4$.

a. "Flip-flopping" shear bands. Near the middle of this line, e.g., $\langle\sigma\rangle=7.0$, we find two "flip-flopping" bands [see Fig. 5(a)]: At any time, the cell is equally divided between a high-stress and a low-stress band, but the identity of the bands reverses periodically. This results in the "checkerboard" spatiotemporal pattern shown in Fig. 5(a). Accordingly, the stress $\sigma(z,t)$, measured for a given height within the cell (e.g., $z=2/3$), displays periodic oscillations with a waveform close to a square wave (and abrupt changes between the low- and high-stress states, as expected for "relaxation oscillations" [54]). The flip-flop period τ_{flip} is of order the structural time τ_S. The shear rate $\dot{\gamma}(t)$ also presents a periodic evolution, albeit with a more complicated waveform. (This extra complexity is generic in our shear rate time series, but seems to be a model-dependent feature rather than connected to any deep physics.)

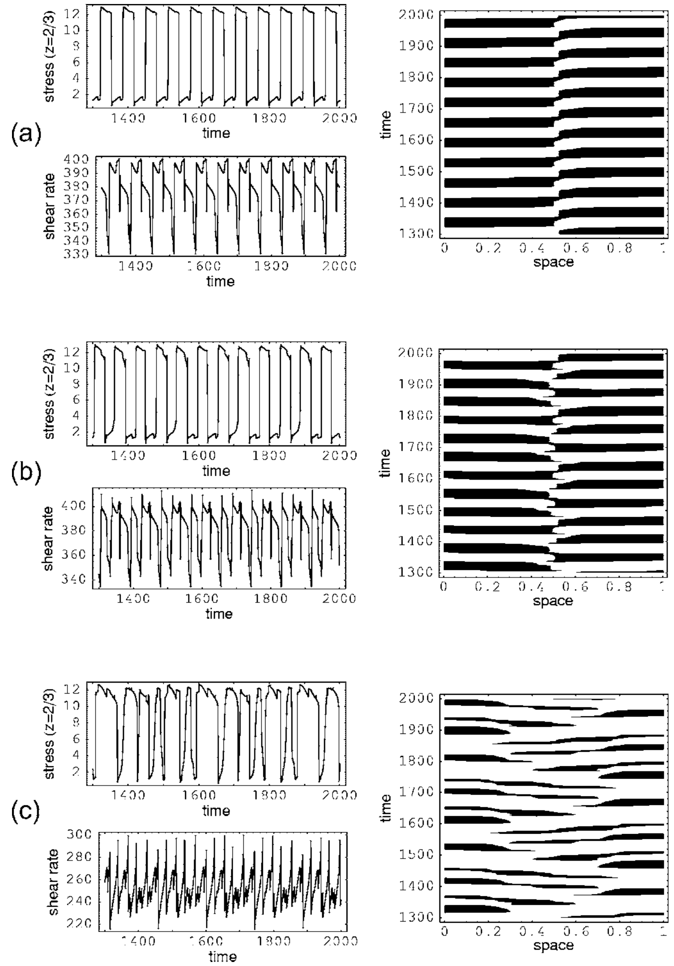

FIG. 5. Typical periodic responses in the oscillating shear band regime, chosen along the line $\tau_S/\tau_M=10^4$ in the phase diagram. (a) Flip-flopping bands at $\langle\sigma\rangle=7$; (b) Zig-zagging interface at $\langle\sigma\rangle=7.1$; (c) Complex periodic motion at $\langle\sigma\rangle=9$. Each group presents time series of the stress σ at $z=2/3$, the shear rate $\dot{\gamma}$, and a space-time plot of $\sigma(z,t)$ with t vertical, z horizontal (clear shades correspond to high stress, dark shades to low stress). Parameters as in Fig. 3.

The mechanism underlying the dynamics of flip-flopping bands is as outlined in Sec. III B: Because of the short-term instability present in the fluid (Fig. 3), shear-bands form. Each of these bands is locally submitted to a van-der-Pol-type instability which forces them to oscillate between states of high and low stress. But these local oscillations cannot occur independently: Because the spatial mean of the stress $\langle\sigma\rangle$ must be conserved, they have to be synchronous—when one band goes up, the other must flip down. Note that shear

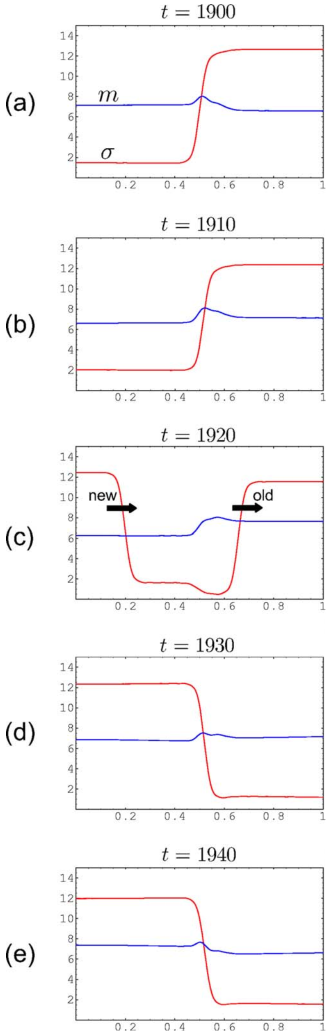

FIG. 6. (Color online) Plots of $\sigma(z,t)$ and $m(z,t)$ vs z for successive times, showing how the "old" interface is replaced with a "new" one in the regime of flip-flopping bands. In (a) and (b) one sees the latency period with stationary interface—note, however, that m slightly evolves from (a) to (b), thus preparing the forthcoming flip; (c) As the flip occurs, traveling wave replacing the previous interface by a new one; (d) and (e) new latency period—note again the slow evolution in m.

bands not only display different values of the stress, but, in general also of the memory $m(z,t)$, albeit much less markedly: In our model, this means that both the mechanical and structural states differ between bands.

Finally, a physically important question in this regime is: What happens to the interface between bands during flip-flops? Looking at Fig. 5(a), we see that the interface position seems stationary. A fixed position for the interface would imply that, in the short interval when bands are flipping, the interface profile has to reverse its slope. Interestingly, closer scrutiny shows that this is *not* what happens: Instead of reversing the slope of a static interface, the system prefers to replace the "wrong" interface by a new one with the correct slope. As seen in Fig. 6, this occurs by a rapid sweeping motion where the old interface quickly travels to one end of the cell and disappears; simultaneously, the new interface is generated at the other end and moves to the middle of the cell, where it will rest until the next flip occurs. Thus, long periods of immobility for the interface alternate with rapid sweeping motions [the latter being too quick to be observable on the scale of the plot in Fig. 5(a)].

Qualitatively, everything happens as though when flips occurs in the bands, they trigger a traveling wave removing the old interface and bringing the new one in. Thus, this regime of flip-flopping bands must be seen as one of intermittent traveling waves, separated by long periods of latency (of order $\tau_S/2$). In accord with this view, when the latency interval diminishes sufficiently (i.e., τ_S is decreased), the intermittent waves should become continuous: This is indeed exactly what happens in the "T"-region of the phase diagram (discussed in Sec. V A 2).

b. Oscillating bands with zig-zagging interface. Pursuing our exploration of the model's behavior along the horizontal line $\tau_S/\tau_M=10^4$, we now move slightly off-center to the right or the left; for example, $\langle\sigma\rangle=7.1$. The interface between bands now adopts a periodic, zig-zagging motion which superposes to the synchronous oscillations of the shear bands [see space-time plot in Fig. 5(b)]. Accordingly, the time series of the stress becomes more complex (square waves are distorted), and the period becomes a multiple (here three) of τ_{flip}. A similar increase in complexity is seen in the shear rate.

The zigzag motion arises because the off-centered value of $\langle\sigma\rangle$ now enforces unbalanced proportions of the low- and high-shear bands in the Couette cell. Because this value for $\langle\sigma\rangle$ is fixed, these proportions are also fixed: Thus each time shear bands oscillate and reverse identities, the interface between them must move to and fro to maintain the required proportions.

c. Complex periodic oscillations. If we now move further towards the wings of the phase diagram, the coupling between the global constraint on $\langle\sigma\rangle$ (unequal bands) and the intrinsic flipping dynamics of the bands generates an extremely complex behavior in the fluid, which, remarkably, manages nonetheless to remain periodic. Figure 5(c) shows the response obtained at $\langle\sigma\rangle=9.0$: The time series for the stress $\sigma(2/3,t)$, though still related to the simple oscillations seen at $\langle\sigma\rangle=7.0$, has become very ragged, and the period is now a large multiple of τ_{flip} (about six times).

We conclude this presentation of regime O by noting that, in experiments, oscillating shear bands similar to our theoretical results have indeed been observed in shear-thickening fluids [11–14].

2. Traveling shear bands

We now describe the second regime in the phase diagram of our model, encountered when τ_S is long as compared to τ_M, but not exceedingly so ($10\leqslant\tau_S/\tau_M\leqslant10^3$; region "T" in Fig. 4). This regime is characterised by a periodic nucleation of shear bands which subsequently cross the system at roughly constant velocity. The typical situation is shown in Fig. 7: Nucleation occurs at a boundary, and bands travel

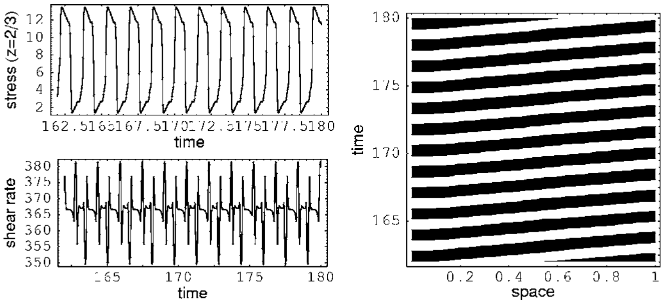

FIG. 7. Periodic time series and space-time plot of the stress $\sigma(z,t)$ in the traveling band regime. Parameters: $\tau_S/\tau_M=90$, $\langle\sigma\rangle=7$, others as in Fig. 3.

across the entire system, one at a time. As before, the period of the various time series is comparable to the structural timescale τ_S. Similar band motion was reported in Ref. [32], but there the bands "ricochet" off the walls of the container.

Figure 8 shows examples of other traveling behaviors in this regime: The first space-time plot (a) presents a case where nucleation occur at a nonboundary point, yielding two outgoing waves in a one-dimensional analogue of the classical "target patterns" seen in chemical oscillators [55]. Space-time plot (b) presents another case of interior nucleation, but where bands alternatively travel to one edge or the other. (Details here strongly depend on the initial conditions.) Finally, space-time plot (c) illustrates how the model behavior crosses over smoothly from oscillating bands in regime O to traveling bands in regime T: The behavior is intermediate between the situations depicted in Fig. 5(a) and Fig. 7, with bands somehow oscillating as they travel.

Note that the waves observed in regime T are kinematic waves, arising from a staggered phase distribution in the local van-der-Pol band oscillations. They are not associated with transport of material or stress; hence the waves can travel through the system boundaries, despite the imposed boundary conditions ($\boldsymbol{\nabla}\sigma=\mathbf{0}$). Accordingly the wave velocity is independent of the stress diffusion constant κ (data not shown).

Finally, we studied how the bands velocity varied as τ_S was changed. At least for the situation in Fig. 7, where there is only one band at a time in the cell, a naive argument for the velocity is as follows. Since traveling bands correspond to (staggered) local oscillations, two successive passages of bands at a given point of the system correspond to the completion of a local oscillation cycle for this point. Noting that the condition of a constant $\langle\sigma\rangle$ imposes that bands disappearing at one end must reappear immediately at the other, we conclude that each band must cross the system in one local oscillation period. Since this is of order τ_S, and recalling that $H=1$, we deduce $v_{\mathrm{band}}\sim 1/\tau_S$ for the band velocity. Our data show that v_{band} indeed decreases with τ_S, and confirm a roughly linear trend with τ_S^{-1} (see Fig. 9).

3. Spatiotemporal rheochaos

The third main regime encountered in the phase diagram arises in two disconnected pockets (regions "C" in Fig. 4) at moderately long values of τ_S relative to τ_M and for strongly

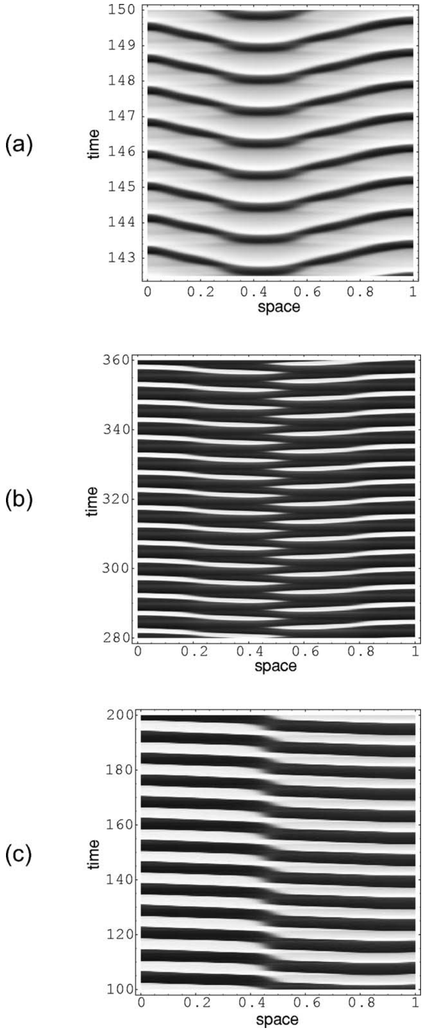

FIG. 8. Space-time plots of the stress $\sigma(z,t)$ showing other examples of traveling bands. (a) "Target pattern" analogue seen at $\tau_S/\tau_M=30$ and $\langle\sigma\rangle=8.5$; (b) Alternating bands seen at $\tau_S/\tau_M=400$ and $\langle\sigma\rangle=5$; (c) Transition between oscillating band and traveling band regime seen at $\tau_S/\tau_M=1000$ and $\langle\sigma\rangle=7$. Other parameters as previously.

off-centered values of the imposed stress $\langle\sigma\rangle$. An increased complexity of oscillations within regime O on approaching the wings of the phase diagram was already noted previously; in regions C, it finally leads to chaotic behavior.

The spatiotemporal patterns produced in this regime are extremely varied and often appear like complex versions of periodic patterns that arise in other parts of the phase diagram. Examples of rheochaos are given in Fig. 10: In Fig. 10(a), we have a regime of chaotic bands with "random defects" between bands (this is similar to rheochaotic patterns observed in shear-thinning micelles in Ref. [32]); in Fig. 10(b), we see a situation which resembles the traveling bands of regime T, but here disordered and following a somewhat wiggling motion; Fig. 10(c) presents the case of flip-flopping bands where irregularities appear within the bands themselves; plot (d) shows traveling bands whose nucleation point changes "at random;" in Figs. 10(e) and 10(f), we observe a "bubbly" phase of localized, short-lived shear bands that appear and disappear erratically in the cell (although

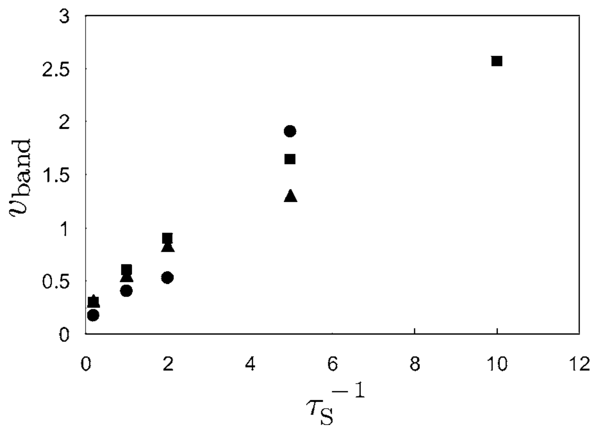

FIG. 9. Velocity of traveling bands vs τ_{S}^{-1}, measured in situations where a single band is present in the system: (●) $\langle\sigma\rangle=8.0$; (■) $\langle\sigma\rangle=7.0$; (▲) $\langle\sigma\rangle=6.0$. The plot shows that v_{band} is roughly proportional to τ_{S}^{-1}. Error bars are ±0.15. Parameters as in previous figures.

occasionally, a band survives and shoots across the system).

Chaos, for each point so marked in Fig. 4, was confirmed by computing the largest Lyapunov exponent, μ_{L}. In Fig. 11, we give a plot of μ_{L} when $\langle\sigma\rangle$ is varied on the horizontal line $\tau_{\mathrm{S}}/\tau_{\mathrm{M}}=20$ of the phase diagram.

Returning to the data of Fig. 10, these patterns vary in how highly developed is the chaos: for instance, Fig. 10(b) seems much more erratic than Fig. 10(c). This is reflected on the Lyapunov exponents: We find $\mu_{\mathrm{L}}\simeq 1.2$ and $\mu_{\mathrm{L}}\simeq 0.2$, respectively. However, we were unable to demonstrate true low-dimensional chaos within our high-order truncation results. Nor could we numerically explore any route to chaos, as the transition window proved unattainably small in the phase diagram. We do however discuss below the route to chaos within the low-order truncation of the model.

A last comment regards the role played by the value of κ, the stress diffusivity, in chaotic regimes. Numerical solutions in this article were computed with a default value of $\kappa=10^{-2}$, but data obtained with different values suggest that smaller values of the stress diffusivity favor chaos. This makes sense, as κ is a damping term for higher Fourier modes [see Eq. (15)]: When κ is smaller, more modes are involved in the dynamics, and thus the system is effectively higher-dimensional. Realistic values for κ might be much smaller than our choice, which was dictated by the need to find N-independent behavior at relatively modest $N\geqslant 25$. Accordingly a more realistic phase diagram at lower κ might display much larger chaotic pockets than Fig. 4.

VI. LOW-ORDER RESULTS

The results presented so far all used a high-order truncation, with a view to obtaining a numerically reliable and precise representation of the continuum model of Eqs. (5) and (6). In this section, we instead study the behavior in the simplest nontrivial mode decomposition of Eqs. (5) and (6), with $N=3$. The corresponding low-dimensional results provide only a caricature of the full dynamics; but they bring interesting insights. This approach is similar in spirit to the classical simplification of the Rayleigh-Bénard equations (describing thermal convection) into the Lorentz equations [56].

By restricting the number of dynamical variables, it permits an analytical or semi-analytical study of some of the model's features. It also clarifies which features of the model survive in low dimension and thus are in some sense robust; we shall see that rheochaos survives the truncation, and is not therefore solely the result of high-order couplings in the full dynamics.

Finally, there are interesting physical consequences to demonstrating the presence of chaos in a low-dimensional Fourier decomposition. The results we have presented so far, along with other works [27,32,33], might be taken to suggest a generic interpretation of rheochaos in complex fluids as resulting from the erratic motion of discrete interfaces between shear bands. This idea is appealing because, in turn, it suggests that rheochaos may be more efficiently modeled by focusing on interfacial dynamics and writing an equation of motion directly for the interface [27,57] (rather than for the whole fluid as we are doing here). The presence of rheochaos in our low-order truncation (which allows only smooth spatial variations of σ and m) shows that sharply defined bands are not an automatic prerequisite for rheochaos.

As already explained in Sec. IV, the lowest possible mode decomposition allowing chaos is obtained for $N=3$. Since the uniform Fourier modes, $\sigma_0=\langle\sigma\rangle$ and m_0, are dynamically inactive, this reduced representation of the model is effectively four-dimensional, with $\sigma_1(t)$, $\sigma_2(t)$, $m_1(t)$, and $m_2(t)$ as the degrees of freedom. Drawing from the general analytical expression given in Appendix B, the dynamical equations for the four retained modes have the relatively simple form (recall $\langle\sigma\rangle$ is a constant):

$$\dot{\sigma}_1=\left[-a+2b\langle\sigma\rangle-3c\langle\sigma\rangle^2-\kappa\left(\frac{\pi}{H}\right)^2\right]\sigma_1-\frac{3}{4}c\sigma_1^3+[b-3c\langle\sigma\rangle]\sigma_1\sigma_2-\frac{3}{2}c\sigma_1\sigma_2^2-\lambda m_1$$

$$\dot{\sigma}_2=\left[-a+2b\langle\sigma\rangle-3c\langle\sigma\rangle^2-\kappa\left(\frac{2\pi}{H}\right)^2\right]\sigma_2-\frac{3}{4}c\sigma_2^3+\frac{1}{2}[b-3c\langle\sigma\rangle]\sigma_1^2-\frac{3}{2}c\sigma_1^2\sigma_2-\lambda m_2$$

$$\dot{m}_1=(\sigma_1-m_1)/\tau_{\mathrm{S}}$$

$$\dot{m}_2=(\sigma_2-m_2)/\tau_{\mathrm{S}}.$$

As with the high-order truncation, we have explored numerically the phase diagram for this minimal model. We indeed find chaos, confirming that rheochaos is a robust feature of the underlying physics. As Fig. 12 shows, the global structure of the phase diagram is also robust and presents the same features as in the high truncation: chaotic behavior appears on both wings of the diagram (off-centered values of $\langle\sigma\rangle$) and for $\tau_{\mathrm{S}}/\tau_{\mathrm{M}}$ ratios not too large (structural relaxation

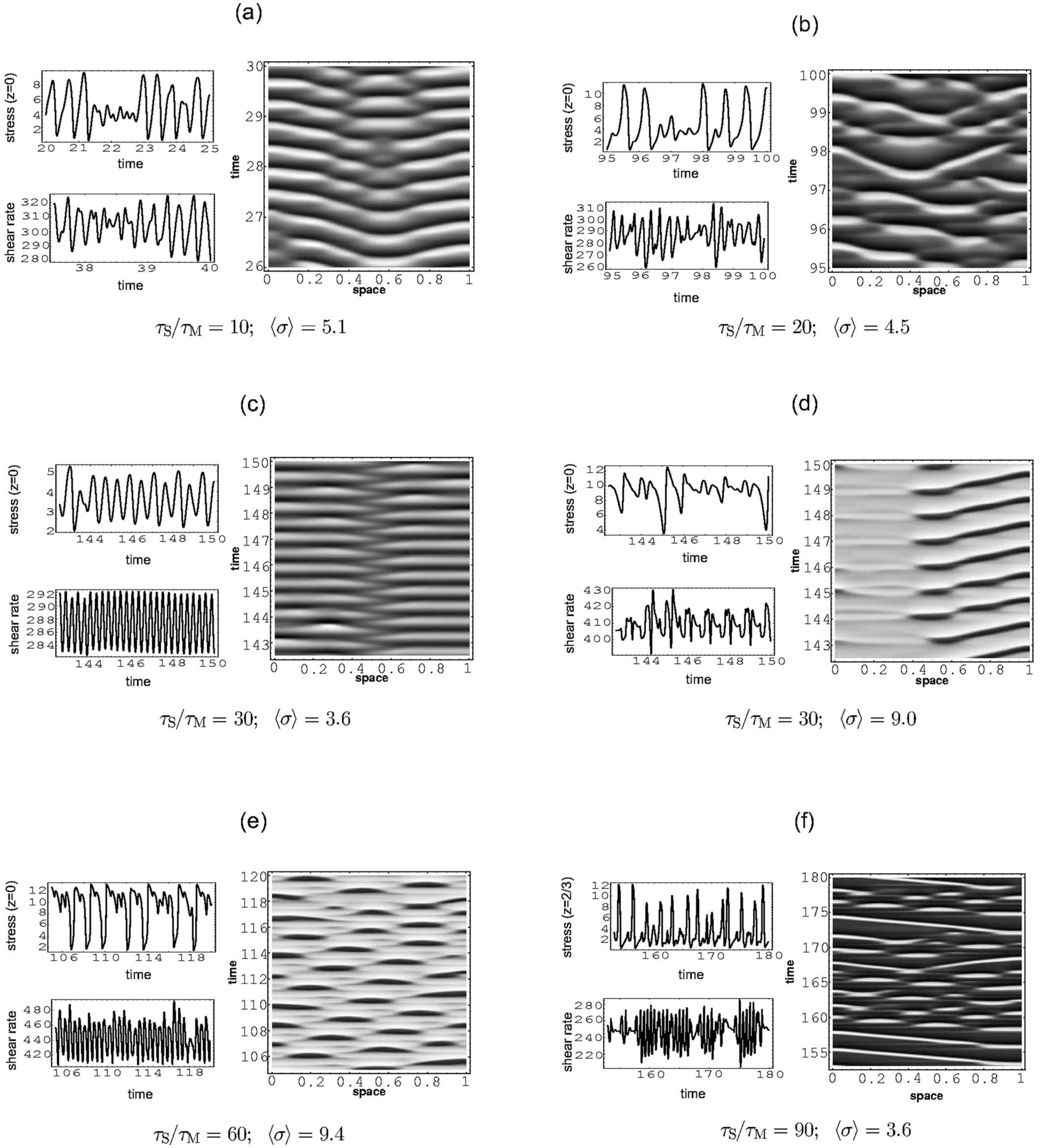

$\tau_S/\tau_M = 10; \;\; \langle\sigma\rangle = 5.1$

$\tau_S/\tau_M = 20; \;\; \langle\sigma\rangle = 4.5$

$\tau_S/\tau_M = 30; \;\; \langle\sigma\rangle = 3.6$

$\tau_S/\tau_M = 30; \;\; \langle\sigma\rangle = 9.0$

$\tau_S/\tau_M = 60; \;\; \langle\sigma\rangle = 9.4$

$\tau_S/\tau_M = 90; \;\; \langle\sigma\rangle = 3.6$

FIG. 10. Various types of spatiotemporal rheochaos observed in the model (high-order truncation). Numerical parameters as in Fig. 3.

not too slow), while periodic states are observed elsewhere. One observation is that chaotic pockets are now much smaller than in the high-order truncation phase diagram: This is natural as chaos is usually facilitated in higher dimensions.

We do not classify periodic points in this low-order model as "oscillating bands" or "traveling bands:" The stress variations are anyway too smooth to allow the definition of proper shear bands. However, as illustrated in Fig. 13, there remain low-dimensional analogues of the oscillating and traveling bands, in roughly the same locations as in the high-order truncation.

In Fig. 14, we show a typical trajectory in the chaotic regime of the low-order model: This appears less erratic than in the high-order counterpart (Fig. 10), essentially amounting to a slightly irregular oscillation of two "bands." The largest Lyapunov exponent is $\mu_L \simeq 0.4$. Finally, we studied the route

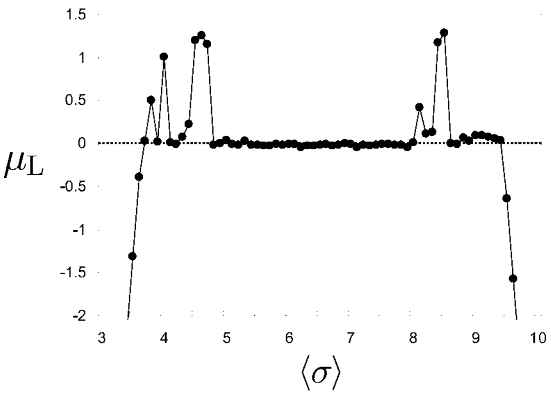

FIG. 11. Plot of the largest Lyapunov exponent μ_L computed as a function of the imposed stress $\langle\sigma\rangle$ on the line $\tau_S/\tau_M=20$ (high-order truncation). Chaotic behavior (positive values) appears only on the wings of the diagram. Imprecision on the exponent values is typically ±0.1. Numerical parameters as in Fig. 3.

to chaos in the low-order truncation, and found a classical period-doubling scenario (Fig. 15). This result does not, however, imply anything about the route to chaos in the high-dimensional version of the model.

The results of this section show, not only that sharp interfaces are not necessary for rheochaos, but also that the low-dimensional representation of our shear-thickening model can reproduce most of the important physical features observed in higher dimensions. This low-order truncation could also enable a deeper understanding of the oscillating and traveling band regimes: We have not explored in detail the relation between τ_{flip}, τ_S, and the band velocity. It might also permit a deeper understanding of the effect of the global stress constraint, particularly the mechanism whereby this affect the dynamics and makes it more or less complex.

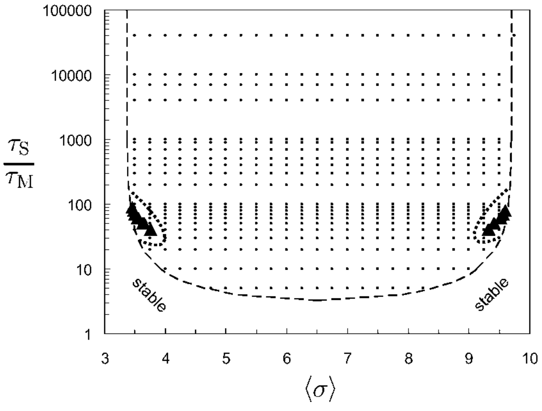

FIG. 12. Phase diagram in the low-dimensional truncation of the model: (●) Periodic points; (▲) Chaotic points. Note that, for pictural clarity, a horizontal spacing between points $\Delta\langle\sigma\rangle=0.25$ was chosen for the plot, but our actual numerical exploration of the phase diagram was performed on a much finer grid with $\Delta\langle\sigma\rangle=10^{-2}$. The outer dashed line delineates the limit of linear stability [Eq. (9)]. Dotted lines around chaotic pockets are merely guides to the eye. Numerical parameters as in Fig. 3.

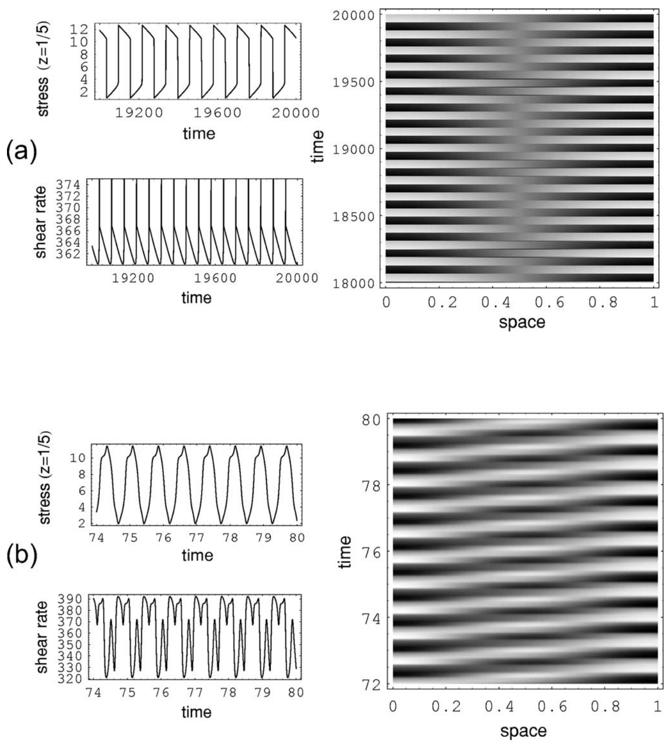

FIG. 13. Low-dimensional analogues to the oscillating band regime (a) and to the traveling band regime (b). Note the ill-defined “interface” between “bands.” Parameters: (a) $\tau_S/\tau_M=10^4$, $\langle\sigma\rangle=7$; (b) $\tau_S/\tau_M=40$, $\langle\sigma\rangle=7$; other parameters as in Fig. 3.

VII. CONCLUSIONS

We have introduced a shear thickening fluid model, allowing for spatial inhomogeneity, in which the relaxation of stress couples to a memory term linked to slow structural changes in the fluid. The interplay between the rheological and the structural dynamics leads to complicated spatio-temporal dynamics. The model maps onto the FitzHugh-Nagumo model for neural networks, but with a different type of global constraint (imposition of the average stress $\langle\sigma\rangle$), specific to complex fluids.

In steady state for both the structure and stress, the flow curve is monotonically increasing. However, short-term flow curves, valid on timescales too short for the structure to re-

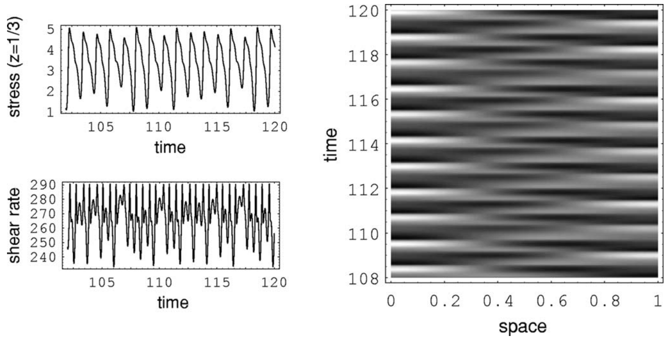

FIG. 14. Rheochaos in the low-dimensional representation of the model, here plotted for $\tau_S/\tau_M=60$ and $\langle\sigma\rangle=3.55$. Numerical parameters as in Fig. 3.

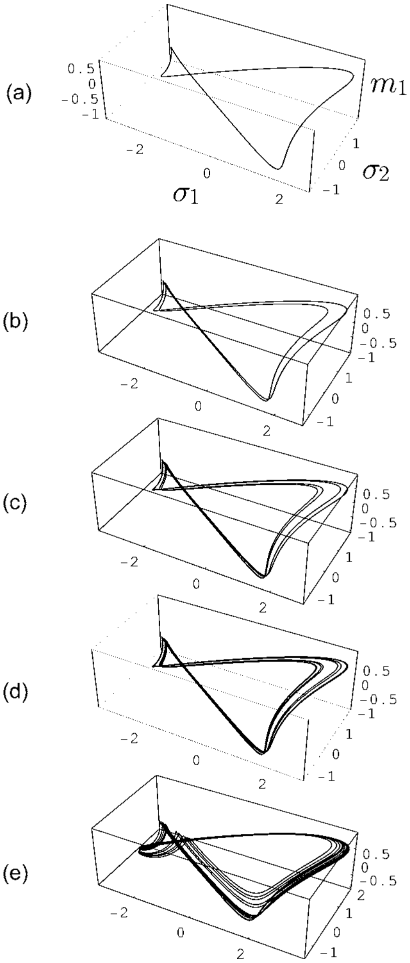

FIG. 15. Route to chaos in the low-dimensional truncation, shown for $\tau_S/\tau_M=60$. Plotted are three-dimensional projection on the (σ_1,σ_2,m_1)-space of the four-dimensional attractors. From (a) to (d), first steps of the period-doubling cascade: (a) $\langle\sigma\rangle=3.53$, (b) $\langle\sigma\rangle=3.535$, (c) $\langle\sigma\rangle=3.5375$, (d) $\langle\sigma\rangle=3.5379$; (e) Chaotic attractor obtained for $\langle\sigma\rangle=3.55$, corresponding to the situation shown in Fig. 14. Numerical parameters as in Fig. 3.

lax, are nonmonotonic and unstable. This obliges the appearance of unsteady shear bands.

The phase diagram of the model on varying $\langle\sigma\rangle$ and the ratio of structural and stress relaxation times, $\tau_S/\tau_M(\geqslant 4)$ has a simple overall structure. Three main regimes were found. For very large τ_S/τ_M, we found oscillating shear bands; elsewhere we found periodic traveling shear bands at mid-range values of $\langle\sigma\rangle$, with regions of spatio-temporal rheochaos for off-center values.

In the oscillating band regime, shear bands must oscillate synchronously while respecting the imposed value for the mean stress $\langle\sigma\rangle$. When the volume fractions of the two bands within the cell are unequal (off-center $\langle\sigma\rangle$) oscillations become increasingly complex but remain periodic. In the other periodic regime seen in the model, bands nucleate at a border point of the container, or more rarely at an interior point, and travel across it at a near-constant velocity which scales roughly as τ_S^{-1}.

Our model exhibits spatio-temporal chaos. The corresponding space-time patterns are varied, but fall into a common picture (coherent with that of other groups [32,33]): Rheochaos manifests as a flow that restlessly attempts to form steady shear bands, but fails due to internal structural constraints.

It is known that the constraint on $\langle\sigma\rangle$ (set by the mechanical torque on a Couette) is essential for shear-thickening fluids as it sets the respective fractions of the high- and low-shear bands in the flow [6]; and that finite stress diffusivity κ provides a selection criterion among possible banded flows [4]. Within our model, the importance of these quantities extends to time-dependent cases: Dynamical complexity increases as $\langle\sigma\rangle$ moves off-center, whereas a smaller diffusivity κ promotes chaos.

Taking advantage of our Fourier-space representation, we also studied a four-dimensional truncation for which we showed that the important physical features found in high dimension persist, including the general structure of the phase diagram.

The presence of chaos in the low-order model shows that sharp interfaces between bands are not necessary for rheochaos. This does not mean that such interfaces have no effect, only that the chaos would persist without them.

In conclusion then, our work, along with others' [32,33], supports a "frustrated shear-banding" picture of rheochaos, in which flow inhomogeneity (whether sharp interfaces or smooth variations) plays a crucial role. A gap between theory and experiment still remains: Our model makes no direct connection with the microscopics of the considered fluids. Improved experimental information about the dimensionality of the observed chaos, or the route into, for shear-thickening systems would be most helpful. One general prediction of our model that may be easily tested experimentally is that the dynamics should get more complex as the imposed stress $\langle\sigma\rangle$ is chosen closer to the edges of the fluid's unstable window.

One potentially important factor that has been neglected in the present model is the role played by normal stresses in the fluid. In many of the experimental fluids we are concerned with, their magnitude is significant in high-shear regimes. One could also consider alternative scenarios for rheochaos, where stress variations do not couple to nonconserved structural changes as proposed here (these include modulation of concentration at finite wavevector, i.e., microphase separation) but instead to conserved modes such as global concentration fields.

ACKNOWLEDGMENTS

The authors thank L. Bécu, A. Colin, S. Fielding, S. Manneville, P. Olmsted, D. Roux, and J.-B. Salmon for discussions. AA funded by EPSRC Grant No. GR/R95098.

APPENDIX A: NON-DIMENSIONALISATION

We here describe how the nondimensional equations (1) and (2) for the model are obtained from the original physical equations. This is especially useful if one wants to deduce the numerical value of a nondimensional parameter used in the model from an experimental value. Throughout this Appendix, we use the convention that normal letters are for dimensional, physical quantities, and starred letters for nondimensional ones. In the rest of the article, all quantities are nondimensional by default, so that stars have systematically been omitted.

The dimensional version of Eq. (1) writes

$$\dot{\sigma} = G\dot{\gamma} - \tau_{\mathrm{M}}^{-1}\sigma + b\sigma^2 - c\sigma^3 - \lambda \int \tau_{\mathrm{S}}^{-1} e^{(t-t')/\tau_{\mathrm{S}}}\sigma(t')dt' + \kappa\nabla_z^2\sigma \tag{A1}$$

where G is the transient elastic modulus, and other quantities have been defined in the main text.

We use G, τ_0 (defined below) and H (the Couette axial extent) as, respectively, the units for stress, time, and space, and define the corresponding reduced quantities: $\sigma^*=\sigma/G$, $t^*=t/\tau_0$, and $z^*=z/H$.

Substituting these quantities in Eq. (A1), we obtain the nondimensional expression

$$\begin{aligned}\dot{\sigma}^* &= \dot{\gamma} - \frac{\tau_0}{\tau_{\mathrm{M}}}\sigma^* + bG\tau_0\sigma^{*2} - cG^2\tau_0\sigma^{*3}\\ &\quad - \lambda\tau_0^2 \int \tau_{\mathrm{S}}^{-1} e^{\tau_0(t^*-t'^*)/\tau_{\mathrm{S}}}\sigma^*(t'^*)dt'^* + \kappa\frac{\tau_0}{H^2}\nabla_{z^*}^2\sigma^*\end{aligned} \tag{A2}$$

We now have to choose a value for the unit time τ_0: For practicality, because we always work on timescales longer than τ_{M}, we choose $\tau_0=100\tau_{\mathrm{M}}$. We next define the reduced Maxwell time $\tau_{\mathrm{M}}^*=\tau_{\mathrm{M}}/\tau_0$ and the constant a^*, its inverse: we have $\tau_{\mathrm{M}}^*=0.01$ and $a^*=\tau_{\mathrm{M}}^{*-1}=100$.

Finally, we transform the remaining physical parameters of the model into reduced quantities: $b^*=bG\tau_0$, $c^*=cG^2\tau_0$, $\lambda^*=\lambda\tau_0$, $\tau_{\mathrm{S}}^*=\tau_{\mathrm{S}}/\tau_0$, $\kappa^*=\kappa\tau_0/H^2$. In terms of these reduced quantities, Eq. (A2) rewrites

$$\begin{aligned}\dot{\sigma}^* &= \dot{\gamma} - a^*\sigma^* + b^*\sigma^{*2} - c^*\sigma^{*3}\\ &\quad - \lambda^* \int \tau_{\mathrm{S}}^{*-1} e^{(t^*-t'^*)/\tau_{\mathrm{S}}^*}\sigma^*(t'^*)dt'^* + \kappa^*\nabla_{z^*}^2\sigma^*\end{aligned}$$

which is exactly the expression given in Eqs. (1) and (2) of the main text (dropping stars out).

APPENDIX B: FULL ANALYTICAL EXPRESSION FOR MODE EQUATIONS

In this Appendix, we give the full analytical expression of the evolution equations for the stress modes $\sigma_n(t)$, of which only a shortened version was given in Eq. (15). [For memory modes, the analytical expression is straightforward and was given in Eq. (16).]

The equation for a given mode σ_n is found by projecting the partial differential equation (5) onto the associated Fourier mode, i.e., by multiplying both sides by $\cos(n\pi z/H)$ and integrating over z. Because the nonlinearities in $R(\sigma)$ are only polynomial, the integrals are analytically tractable. (Note that this is a rare fact in spectral or pseudo-spectral schemes; when nonlinearities are more complex, in general, exact expressions for mode equations do not exist, and the numerical scheme accordingly increases in complexity [50].) The only difficulty in the present case comes from the fact that we deal with truncated Fourier series (this explains some rather baroque expressions for summation limits in the following).

Considering a truncation of order N (i.e., the highest mode is σ_{N-1}), the governing equation for the evolution of mode $\sigma_n(t)$ writes (for all n such that $0\leqslant n\leqslant N-1$):

$$\begin{aligned}\dot{\sigma}_n &= \delta_n^0\dot{\gamma} - a\sigma_n + \frac{b}{2}\sum_{p=0}^{n}\sigma_p\sigma_{n-p} + (2-\delta_n^0)\frac{b}{2}\sum_{p=0}^{N-1-n}\sigma_p\sigma_{p+n}\\ &\quad - \frac{c}{4}\sum_{p=0}^{n}\sum_{q=0}^{n-p}\sigma_p\sigma_q\sigma_{n-p-q} - \frac{c}{4}\sum_{p=0}^{N-1}\sum_{q=q_1}^{q_2}\sigma_p\sigma_q\sigma_{n+p-q}\\ &\quad - (3-2\delta_n^0)\frac{c}{4}\sum_{p=0}^{N-1-n}\sum_{q=0}^{N-1-n-p}\sigma_p\sigma_q\sigma_{n+p+q} - (2-\delta_n^0)\\ &\quad \times\frac{c}{4}\sum_{p=0}^{N-1}\sum_{q=q_3}^{q_4}\sigma_p\sigma_q\sigma_{n+q-p} - \lambda m_n - \kappa\left(\frac{n\pi}{H}\right)^2\sigma_n\end{aligned}$$

where δ is the usual Kronecker symbol, and the following shorthands were used

$$q_1 = \max\{n+p-N+1,0\}$$

$$q_2 = N-1+\min\{n+p-N+1,0\}$$

$$q_3 = \max\{0,p-n\}$$

$$q_4 = N-1+\min\{0,p-n\}.$$

In high-order truncations ($N=40$), a typical mode equation contains several hundreds terms. Note also that the zeroth-mode equation ($n=0$) is the only one where the shear rate $\dot{\gamma}$ appears; since, in addition, we have $\dot{\sigma}_0=\frac{\mathrm{d}}{\mathrm{d}t}\langle\sigma\rangle=0$ under conditions of fixed torque, this equation can be used to compute $\dot{\gamma}(t)$ from the individual stress modes $\sigma_n(t)$. This is in fact the same equation as Eq. (20), but here the integral has been calculated explicitly.

---

[1] R. G. Larson, *The Structure and Rheology of Complex Fluids* (Oxford University Press, Oxford, 1999).

[2] M. E. Cates, in *Slow Relaxations and Nonequilibrium Dynamics in Condensed Matter, Les Houches Session LXXVII*, edited by J.-L. Barrat, M. Feigelman, J. Kurchan, and J. Dalibard (Springer, New York, 2003).

[3] N. A. Spenley, M. E. Cates, and T. C. B. McLeish, Phys. Rev. Lett. **71**, 939 (1993).

[4] C.-Y. David Lu, P. D. Olmsted, and R. C. Ball, Phys. Rev. Lett. **84**, 642 (2000).

[5] P. D. Olmsted, Europhys. Lett. **48**, 339 (1999).
[6] J. L. Goveas and P. D. Olmsted, Eur. Phys. J. E **6**, 79 (2001).
[7] P. G. Drazin and W. H. Reid, *Hydrodynamic Stability* (Cambridge University Press, Cambridge, 2004).
[8] P. Manneville, *Instabilities, Chaos and Turbulence* (Imperial College Press, London, 2004).
[9] A. Groisman and V. Steinberg, Nature (London) **405**, 53 (2000).
[10] Y. T. Hu, P. Boltenhagen, E. Matthys, and D. J. Pine, J. Rheol. **42**, 1209 (1998).
[11] E. K. Wheeler, P. Fischer, and G. G. Fuller, J. Non-Newtonian Fluid Mech. **75**, 193 (1998).
[12] P. Fischer, Rheol. Acta **39**, 234 (2000).
[13] P. Fischer, E. K. Wheeler, and G. G. Fuller, Rheol. Acta **41**, 35 (2002).
[14] V. Herle, P. Fischer, and E. J. Windhab, Langmuir **21**, 9051 (2005).
[15] A.-S. Wunenburger, A. Colin, J. Leng, A. Arnéodo, and D. Roux, Phys. Rev. Lett. **86**, 1374 (2001).
[16] J.-B. Salmon, A. Colin, and D. Roux, Phys. Rev. E **66**, 031505 (2002).
[17] S. Manneville, J.-B. Salmon, and A. Colin, Eur. Phys. J. E **13**, 197 (2004).
[18] L. Courbin, P. Panizza, and J.-B. Salmon, Phys. Rev. Lett. **92**, 018305 (2004).
[19] L. Hilliou and D. Vlassopoulos, Ind. Eng. Chem. Res. **41**, 6246 (2002).
[20] H. M. Laun, J. Non-Newtonian Fluid Mech. **54**, 87 (1994).
[21] R. Bandyopadhyay, G. Basappa, and A. K. Sood, Phys. Rev. Lett. **84**, 2022 (2000).
[22] R. Bandyopadhyay and A. K. Sood, Europhys. Lett. **56**, 447 (2001).
[23] W. M. Holmes, M. R. López-González, and P. T. Callaghan, Europhys. Lett. **64**, 274 (2003).
[24] M. R. López-González, W. M. Holmes, P. T. Callaghan, and P. J. Photinos, Phys. Rev. Lett. **93**, 268302 (2004).
[25] J.-B. Salmon, S. Manneville, and A. Colin, Phys. Rev. E **68**, 051504 (2003).
[26] D. Lootens, H. Van Damme, and P. Hébraud, Phys. Rev. Lett. **90**, 178301 (2003).
[27] M. E. Cates, D. A. Head, and A. Ajdari, Phys. Rev. E **66**, 025202 (2002).
[28] A. Aradian and M. E. Cates, Europhys. Lett. **70**, 397 (2005).
[29] A. Aradian and M. E. Cates, in *Proc. of the 3rd Int. Symp. on Slow Dynamics in Complex Systems*, edited by M. Tokuyama and I. Oppenheim (American Institute of Physics, Melville, NY, 2004), AIP Conference Proceedings, Vol. 708.
[30] C. B. Holmes, M. E. Cates, M. Fuchs, and P. Sollich, J. Rheol. **49**, 237 (2005).
[31] M. E. Cates and S. J. Candau, Europhys. Lett. **55**, 887 (2001).
[32] S. M. Fielding and P. D. Olmsted, Phys. Rev. Lett. **92**, 084502 (2004).
[33] B. Chakrabarti, M. Das, C. Dasgupta, S. Ramaswamy, and A. K. Sood, Phys. Rev. Lett. **92**, 055501 (2004).
[34] *Soft and Fragile Matter: Nonequilibrium Dynamics, Metastability and Flow*, edited by M. R. Evans and M. E. Cates, (Institute of Physics Publishing, Bristol, 2000).
[35] P. Sollich, F. Lequeux, P. Hébraud, and M. E. Cates, Phys. Rev. Lett. **78**, 2020 (1997).
[36] D. A. Head, A. Ajdari, and M. E. Cates, Phys. Rev. E **64**, 061509 (2001).
[37] C. Derec, A. Ajdari, and F. Lequeux, Eur. Phys. J. E **4**, 355 (2001).
[38] S. M. Fielding, Phys. Rev. Lett. **95**, 134501 (2005).
[39] For completeness, we also explored the behavior of the model of Eq. (1) under conditions (unusual for vorticity banding) of imposed shear rate. In all runs, without exception, the response proved purely temporal: In contrast with our results under imposed stress discussed in the main text, here the dynamics in the system converges very early on to a situation where all points are in the same state at any given instant of time and oscillate in synchrony over space. The only observable instability thus corresponds to global, periodic oscillations of the system (no shear bands nor rheochaos). The effective dynamics for each point in the cell is simply that seen in the earlier, temporal version of the model proposed in Ref. [27].
[40] P. M. Chaikin and T. C. Lubensky, *Principles of Condensed Matter Physics* (Cambridge University Press, Cambridge, 1995).
[41] J. D. Murray, *Mathematical Biology*, 3rd ed. (Springer Verlag, New York, 2002).
[42] R. FitzHugh, Biophys. J. **1**, 445 (1961).
[43] J. Nagumo, S. Arimoto and S. Yoshizawa, Proc. IRE **50**, 2061 (1962).
[44] J. Keener and J. Sneyd, *Mathematical Physiology* (Springer Verlag, New York, 1998).
[45] C. Rocsoreanu, A. Georgescu, and N. Giurgiteanu, *The FitzHugh-Nagumo model* (Kluwer Academic Publishers, Amsterdam, 2000).
[46] J. A. Acebrón, A. R. Bulsara, and W.-J. Rappel, Phys. Rev. E **69**, 026202 (2004).
[47] G. Baier and M. Müller, Rev. Mex. Fis. **50**, 422 (2004).
[48] C. G. Assisi, V. K. Jirsa, and J. A. Scott Kelso, Phys. Rev. Lett. **94**, 018106 (2005).
[49] M. A. Zaks, X. Sailer, L. Schimansky-Geier, and A. B. Neiman, Chaos **15**, 026117 (2005).
[50] S. M. Fielding and P. D. Olmsted, Eur. Phys. J. E **11**, 65 (2003).
[51] J. P. Boyd, *Chebyshev and Fourier Spectral Methods* (Dover Publications, New York, 2000).
[52] A. W. El-Kareh and L. G. Leal, J. Non-Newtonian Fluid Mech. **33**, 257 (1989).
[53] MATHEMATICA, Version 5.0 (Wolfram Research, Inc., Champaign, 2003).
[54] P. Glendinning, *Stability, Instability and Chaos* (Cambridge University Press, Cambridge, 1994).
[55] I. R. Epstein and J. A. Pojman, *An Introduction to Nonlinear Chemical Dynamics* (Oxford University Press, Oxford, 1998).
[56] P. Manneville, *Dissipative Structures and Weak Turbulence* (Academic Press, New York, 1990).
[57] A. Ajdari, Phys. Rev. E **58**, 6294 (1998).